

Research Article

Investigation of Optical and Dielectric Properties of Nickel-Doped Zinc Oxide Nanostructures Prepared via Coprecipitation Method

Sohail Ahmad ¹, Muhammad Usman ¹, Muhammad Hashim ¹, Atizaz Ali ¹,
Rasool Shah ², and Naveed Ur Rahman ³

¹Department of Physics, Abdul Wali Khan University Mardan, Mardan, Khyber Pakhtunkhwa, Pakistan

²Department of Computer Science and Mathematics, Lebanese American University, Beirut, Lebanon

³Department of Physics, Bacha Khan University Charsadda, Charsadda, Khyber Pakhtunkhwa, Pakistan

Correspondence should be addressed to Rasool Shah; rasool.shah@lau.edu.lb and Naveed Ur Rahman; dr.naveed@bkuc.edu.pk

Received 10 November 2023; Revised 13 January 2024; Accepted 5 February 2024; Published 16 February 2024

Academic Editor: Nico Lovergine

Copyright © 2024 Sohail Ahmad et al. This is an open access article distributed under the Creative Commons Attribution License, which permits unrestricted use, distribution, and reproduction in any medium, provided the original work is properly cited.

Nanostructures of undoped zinc oxide and nickel-doped zinc oxide ($\text{Ni} = \text{Zn}_{0.98}\text{Ni}_{0.02}\text{O}$, $\text{Zn}_{0.96}\text{Ni}_{0.04}\text{O}$, and $\text{Zn}_{0.94}\text{Ni}_{0.06}\text{O}$) were synthesized by using the coprecipitation process, and their optical and dielectric properties were simultaneously investigated. The XRD results confirm the hexagonal structure having space group P63mc. By increasing nickel concentration, the particle size decreases, while the strain is increased. Fourier-transform infrared (FTIR) analysis was carried out in order to learn more about the phonon modes present in nickel-doped zinc oxide. UV-Vis spectroscopy further revealed that the optical band gap of nickel-doped samples varied from 3.18 eV to 2.80 eV. The SEM analysis confirms the rod shape morphology of the already synthesized samples. EDX analysis investigates the incorporation of nickel ions into the zinc oxide lattice. Using photoluminescence spectroscopy, we found that the synthesized materials had oxygen vacancies (Vo) and zinc interstitial (Zn_i) defects. Dielectric constant (ϵ_r) and dielectric loss (ϵ'') are both improved in nickel-doped zinc oxide compared to undoped zinc oxide. Since more charge carriers enhanced after the nickel ions were exchanged for the Zn ions, the AC electrical conductivity ($\sigma_{a.c}$) improves by nickel doping compared to undoped zinc oxide.

1. Introduction

Transition metal oxide compounds have some special characteristics among which zinc oxide is an interesting n-type semiconductor with a wide band gap of 3.37 eV and a maximum exciton binding energy of 60 meV. Due to its unique properties like nontoxicity, easy synthesis, low cost, and good electrical and thermal stability, it is a promising compound for various optoelectronic applications, i.e., solar cells [1–3], UV photo detectors [4], UV absorbers [5], LEDs [6–8], capacitors, battery electrodes [9], sensors [10–12], resonators, and TCO [13], and also can be used as photocatalyst [14].

For various optoelectronic purposes, zinc oxide is doped with transition metals (Fe, Co, Ni, Cu, etc.) among which nickel is the most promising candidate due to its extreme stability. Numerous research studies have been conducted to

explore the different properties of zinc oxide through a number of dopants. However, nickel-doped zinc oxide is a good candidate owing to its good photonic ability, high electrical conductivity, and good chemical stability. Therefore, nickel-doped zinc oxide has high dielectric constant and low dielectric loss as compared to undoped zinc oxide and has significant electrical conductivity which makes it a promising candidate for optoelectronic applications. The introduction of various defects in metal oxides has a great influence on their band structure and donor densities and hence influences optical and dielectric properties [15]. Zinc oxide exhibits numerous induced defects, with the most favorable ones being the oxygen vacancies labeled as Vo [16]. Many experimental and theoretical works showed that the electronic charge transport, band structure, and surface properties are mostly attributed to Vo . The improvement in charge generation and separation is attributed to the

presence of isolated energy levels resulting from the influence of Vo [17, 18]. In addition, oxygen vacancies are recognized as dynamic sites for surface adsorption and desorption phenomena [19, 20]. Recently, a lot of research was carried out for the stable synthesis of zinc oxide for investigating its optical and dielectric behavior.

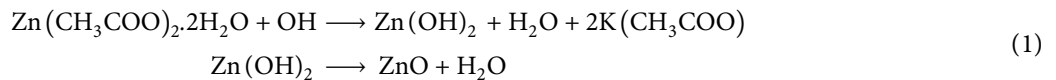
Many routes like hydrothermal method [21], metal organic chemical vapor deposition [22], polyol method [4, 23], sol-gel [24], solution combustion [25], coprecipitation [26, 27], carbothermal evaporation [28], and electrodeposition [29] methods are used to synthesize zinc oxide nanostructures. Among the mentioned methods, the coprecipitation method has the advantage of greater yield, low temperature synthesis, and greater reaction properties. In the present work, we have prepared pure and nickel-doped zinc oxide nanostructures via the chemical coprecipitation method. The aim of the study is to investigate the optical and dielectric properties of the prepared samples for various optoelectronic applications. Nickel-doped zinc oxide nanostructures showed enhanced dielectric constant, high electrical conductivity, and low dielectric loss due to various defects such as V_o and Zn_i . It is noteworthy that, prior to this, there had been limited research on oxygen vacancies to demonstrate the optical and dielectric properties of nickel-doped zinc oxide [30–32]. Hence, our explored results show that nickel-doped zinc oxide can be a favorable candidate for various optoelectronic applications.

2. Experimental

2.1. Chemicals. Zinc acetate dihydrate [$Zn(CH_3COO)_2 \cdot 2H_2O$], nickel chloride hexahydrate ($NiCl_2 \cdot 6H_2O$), KOH, and DI water were used for the preparation of samples. All the chemicals were purchased from Sigma-Aldrich with 99% purity.

2.2. Sample Preparation. The pure zinc oxide and $Zn_{0.98}Ni_{0.02}O$, $Zn_{0.96}Ni_{0.04}O$, and $Zn_{0.94}Ni_{0.06}O$ nickel-doped samples were synthesized by the chemical wet coprecipitation method.

2.202 g of zinc acetate dihydrate [$Zn(CH_3COO)_2 \cdot 2H_2O$] was dissolved in 100 ml DI water, and then 1.125 g of KOH was dissolved in 10 ml DI water. The KOH solution was dropwise added to the zinc acetate solution under vigorous stirring. The precipitate was then put on hot plate for 3 hours at 70°C. The temperature was kept constant, and the reaction was carried out. The obtained white precipitate was then washed with DI water by centrifugation and then dried at 80°C for 24 hours. The prepared powder was then annealed in a furnace for 4 hours at 600°C. The same experiment was performed several times, and the same results were obtained with controlled synthesis. The synthesis diagram is given in Figure 1. The chemical reaction is given below:



2.3. Characterization Tools. The structural properties of the prepared samples were carried out through JEOL-3522 X-ray diffractometer with aCu- α ($\lambda = 1.54057\text{\AA}$) operated at 40 kV in the range of 20 and 80 2θ values. The morphological study was carried out through a conventional MIRA3 TESCAN SEM operated at 15 KV. The chemical composition was studied through EDX spectroscopy attached to SEM. The absorption spectra were studied through UV-Vis PEAK spectrometer at the wavelength range of 200–800 nm and the luminescence emission spectra was carried out through Edinburgh FS5 luminescence spectrometer with a Xenon lamp as the excitation source. Vibrational bondings were studied through FTIR spectroscopy and PerkinElmer spectrometer was used at range of 400–4000 cm^{-1} .

Frequency-dependent dielectric properties and AC conductivity were examined by using an impedance analyzer (MICROTEST 6630) at 10–10 MHz frequency range.

3. Results and Discussion

3.1. X-Ray Diffraction Analysis. Figure 2(a) shows the XRD pattern of the undoped zinc oxide and nickel-doped zinc oxide. The 2θ values were recorded between the ranges of 20

to 80° using X-ray diffractometer. The d-spacing corresponds to the standard JCPDS card number 01-089-0510 for zinc oxide. The figure reveals that the peaks in the pattern align with the hexagonal structure of zinc oxide wurtzite planes. From the 2θ values, the interplanar spacing values are calculated and are listed in Table 1. All the observed peaks correspond to (100), (002), (101), (102), (110), (103), (200), (112), and (201) planes of zinc oxide, and no other impurity peaks are observed related to nickel, oxide of nickel, and Zn impurity phases. This is because nickel (0.69°A) [31] has a smaller ionic radius than that of Zn (0.74°A) [31], so with doping, no extra peaks were observed, and due to the small ionic radius of nickel, it did not change the wurtzite structure. A shift of about 0.12° in the XRD pattern of nickel-doped zinc oxide was observed towards higher angle which confirms the incorporation of the nickel ions into the zinc oxide matrix as seen in Figure 2(b). The cell volumes were found by the following formula [32]:

$$\begin{aligned} V &= \sqrt{\frac{3}{2}} a^2 c \\ &= 0.866 a^2 c, \end{aligned} \quad (2)$$

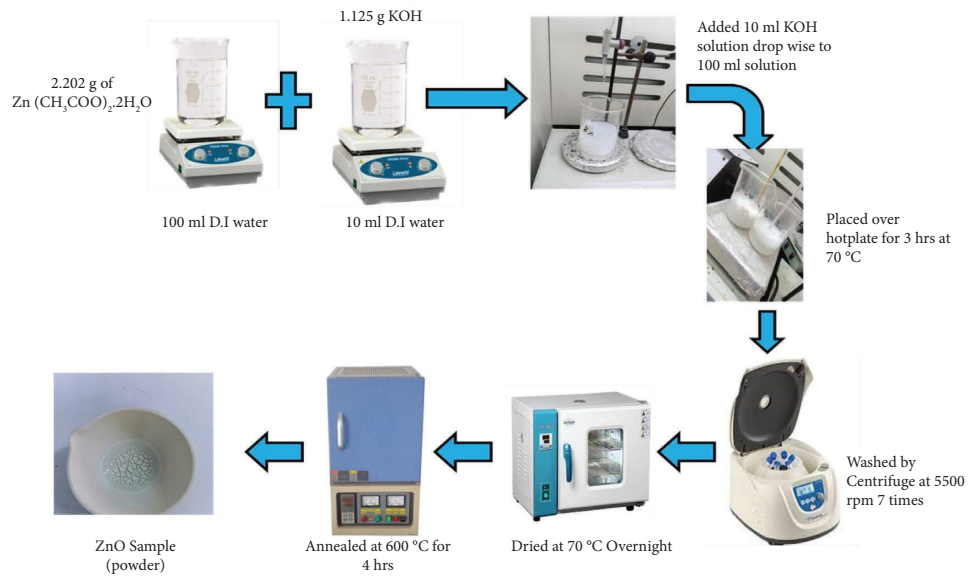


FIGURE 1: Synthesis diagram for the preparation of undoped and nickel-doped zinc oxide.

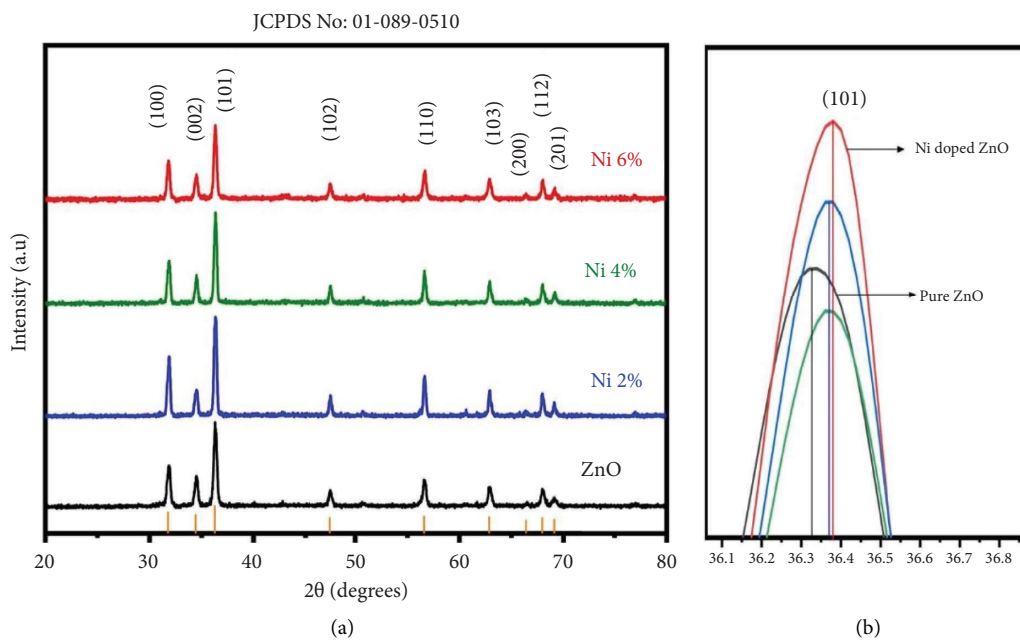


FIGURE 2: Continued.

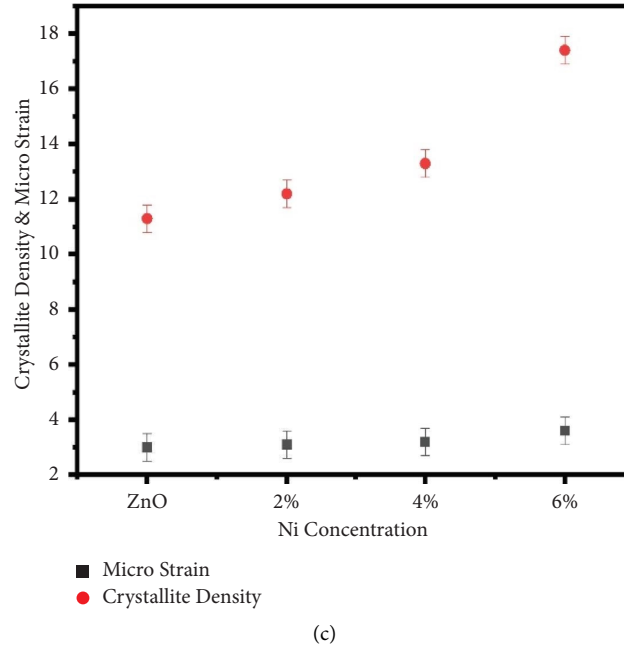


FIGURE 2: (a) XRD pattern of undoped and nickel-doped zinc oxide. (b) Shift in XRD. (c) Microstrain and crystallite density.

TABLE 1: Different lattice parameters of pure zinc oxide and nickel-doped zinc oxide.

Sample	$a = b$ (Å)	c (Å)	Cell volume (Å) ³	Crystallite size (nm)	Microstrain $\times 10^{-4}$	Crystallite density (cm) ⁻²	E_g (eV)
ZnO	3.2507	5.2087	48	30 \pm 1	3.0	1.1 $\times 10^{11}$	3.18
Zn _{0.98} Ni _{0.02} O	3.2502	5.2080	48	28 \pm 1	3.1	1.2 $\times 10^{11}$	3.12
Zn _{0.96} Ni _{0.04} O	3.2496	5.2077	47	27 \pm 1	3.2	1.3 $\times 10^{11}$	2.90
Zn _{0.94} Ni _{0.06} O	3.2471	5.2061	47	24 \pm 1	3.6	1.7 $\times 10^{11}$	2.80

where a and c are the lattice constants. It was observed that the volume of the nickel-doped samples was reduced as compared to the undoped zinc oxide. This occurs because nickel possesses smaller ionic radii (0.69 Å) compared to Zn (0.74 Å), leading to a reduction in lattice constants and consequently, a decrease in cell volume. The Debye–Scherrer equation (33) is used to calculate the crystallite size. The reported crystallite size values are lower-bound estimates.

$$D = \frac{k\lambda}{\beta \cos \theta} \quad (3)$$

where constant $K = 0.94$, λ is the wavelength of incident X-ray, β is the full width at half maximum (FWHM), θ is the diffraction angle, and D is the crystallite size. The average crystallite size varies from 30 to 23 nm for undoped and nickel-doped zinc oxide, respectively. The reduction in the crystallite size is due to small ionic radii of nickel and the nickel-induced strain. Microstrain is calculated from the following formula [34]:

$$\varepsilon = \frac{\beta_{hkl}}{4 \tan \theta} \quad (4)$$

By utilizing the formula mentioned above, it was noticed that a decrease in crystallite size and an increase in nickel concentration resulted an increase in the calculated strain

from 3×10^{-4} to 3.6×10^{-4} [31]. The crystallite density is calculated from the following formula [34, 35]:

$$\sigma = \frac{1}{D^2} \quad (5)$$

The calculated crystallite density varies from $1.1 \times 10^{11}(\text{cm})^{-2}$ to $1.7 \times 10^{11}(\text{cm})^{-2}$ for undoped and nickel-doped zinc oxide, respectively. Different lattice parameters are shown in Table 1. Crystallite density versus microstrain graph is given in Figure 2(c).

3.2. SEM and EDX Analysis. Morphological and elemental composition study was carried out through scanning electron microscopy. Figure 3 shows the SEM micrographs of undoped and nickel-doped zinc oxide. From the SEM micrographs, it is clear that rod-like morphologies are formed for both the undoped and nickel-doped samples. The rods showed some variability which is due to the doping of Ni into ZnO lattice. The particle size was seen to decrease with increasing nickel concentration, and the same was reported in [36, 37].

The elemental composition was studied through EDX analysis, and the results show that there are Zn, and O, and Zn, O, and nickel ions present in the undoped and nickel-doped zinc oxide, respectively, which also confirmed the successful

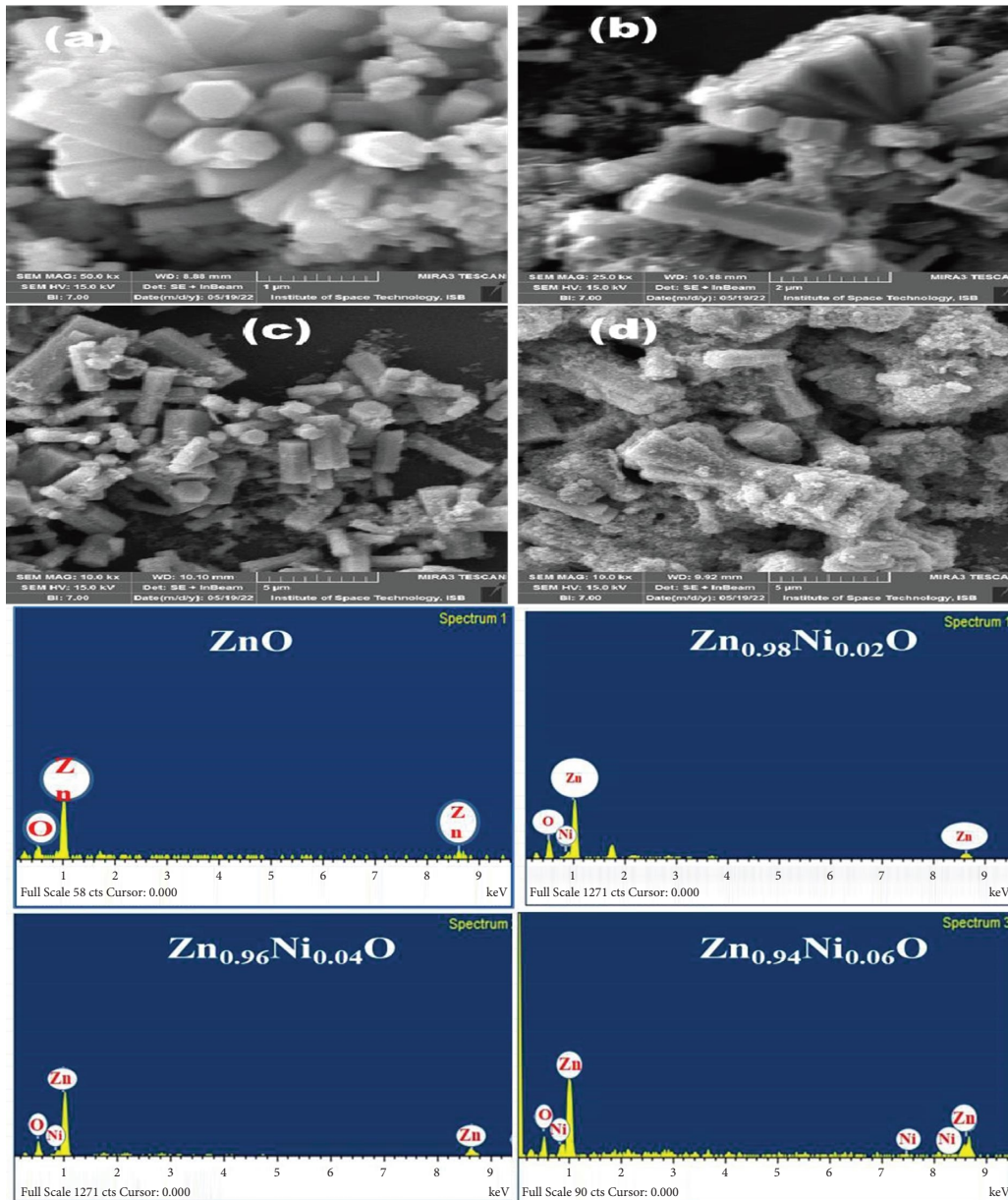


FIGURE 3: (a–d) SEM images of pure and nickel-doped zinc oxide and the other four are EDX images of pure and nickel-doped zinc oxide.

induction of nickel ions into the zinc oxide lattice. No extra impurities were detected which confirm the high purity of the samples. The quantitative analysis is given in Table 2.

3.3. Fourier-Transform Infrared (FTIR) Spectroscopy. The Ni-zinc oxide wurtzite structure was further supported by FTIR analysis. The FTIR recorded spectra were between 400 and 4000 cm^{-1} as shown in Figure 4. The absorption peak around 460 cm^{-1} [31] is attributed to Zn-O symmetric stretching mode. Another peak around 570 cm^{-1} is assigned to Zn-O asymmetric stretching mode. The absorption peaks were shifted to higher wavenumber values which confirm the doping of nickel into the zinc oxide. A small absorption peak around 2360 cm^{-1} is observed as well which corresponds to CO_2 molecules present in the air.

3.4. UV-Vis Spectroscopy. The UV-Vis absorption spectra of undoped and nickel-doped zinc oxide were carried out through UV-Vis spectrometer in the 300–800 nm wavelength range as given in Figure 5(a). Generally, the position of absorbance value depends on the size of the nanoparticles, oxygen deficiency, grain structure, band gap, etc. The absorption band edge in undoped zinc oxide occurs at 367 nm and that in nickel-doped zinc oxide occurs at 369–375 nm which was slightly shifted towards longer wavelengths. This shows that the band gap has decreased with nickel doping. The peaks due to nickel doping are attributed to d-d transition bonds [32], which is the property of nickel in octahedral symmetry. These electronic transitions confirm that Zn is substituted by nickel into the octahedral zinc oxide lattice. Tauc relation was used to calculate the optical energy band gap.

TABLE 2: EDX quantitative analysis of undoped and nickel-doped zinc oxide.

Element	Weight (%)	Atomic (%)
<i>ZnO</i>		
Zn (L)	80.80	50.73
O (K)	19.20	49.27
<i>Zn_{0.98}Ni_{0.02}O</i>		
Zn (L)	80.23	50.10
O (K)	19.00	49.43
Ni (K)	0.77	0.47
<i>Zn_{0.96}Ni_{0.04}O</i>		
Zn (L)	77.47	48.76
O (K)	18.94	48.72
Ni (K)	3.59	2.52
<i>Zn_{0.94}Ni_{0.06}O</i>		
Zn (L)	77.06	46.32
O (K)	17.15	48.95
Ni (K)	5.79	4.73

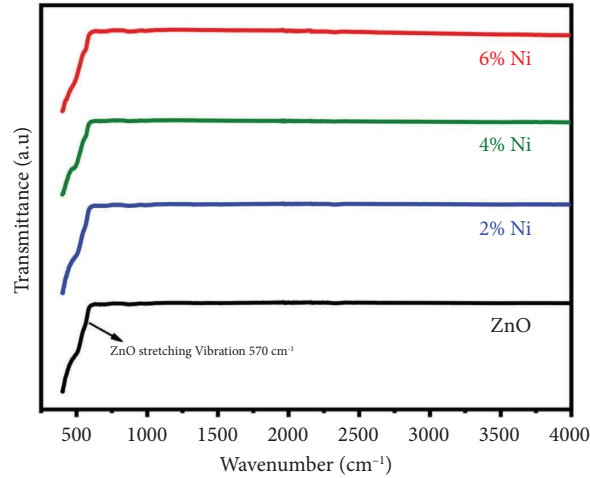


FIGURE 4: FTIR spectra of undoped and nickel-doped zinc oxide.

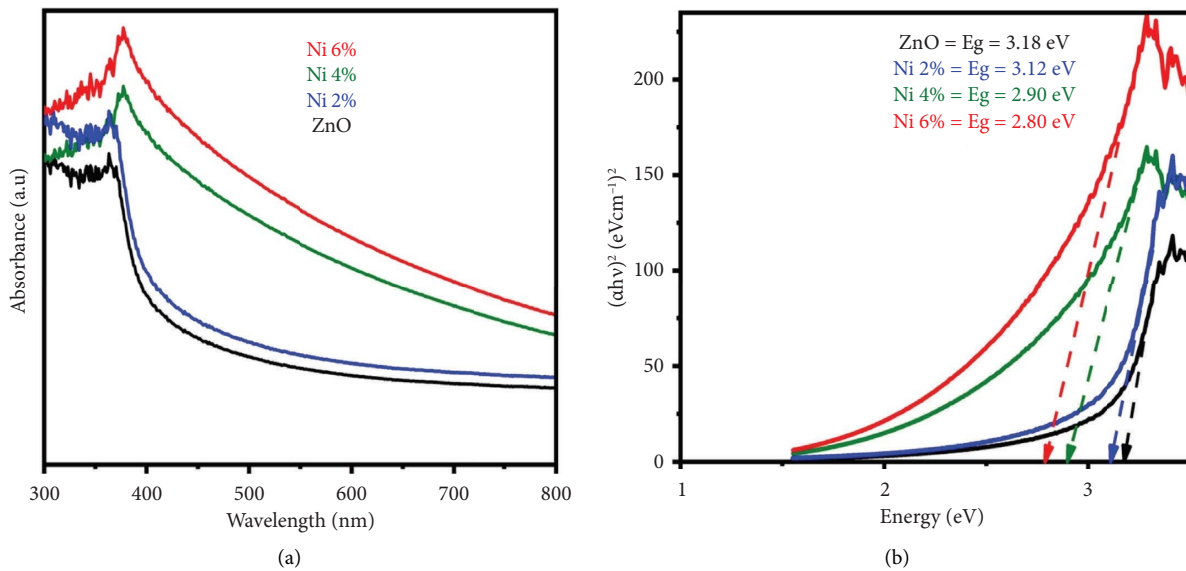


FIGURE 5: (a) UV-Vis absorption spectra. (b) Tauc plot of both undoped and nickel-doped zinc oxide.

$$(\alpha h\nu)^n = A(h\nu - E_g), \quad (6)$$

where $h\nu$, α , and E_g are the photon energy, absorption coefficient, and band energy, respectively, and n corresponds to the type of transition. The band gap was calculated by plotting $(\alpha h\nu)^2$ versus $h\nu$ and then the linear part of the absorption edge was extrapolated to find the intercept with energy axis as shown in Figure 5(b). The band gap calculated was 3.18 eV for undoped zinc oxide and 3.12 eV, 2.90 eV, and 2.80 eV for $\text{Zn}_{0.98}\text{Ni}_{0.02}\text{O}$, $\text{Zn}_{0.96}\text{Ni}_{0.04}\text{O}$, and $\text{Zn}_{0.94}\text{Ni}_{0.06}\text{O}$ nickel-doped zinc oxide, respectively. The d electron of nickel and the s and p electrons [32] of the host matrix are known to have a strong exchange contact, which may be responsible for the narrowing of the band gap through sp-d exchange interactions [38]. The wurtzite structure of zinc oxide is unaffected by the presence of Ni^{2+} ions in the divalent valency state in an octahedral crystal field.

3.5. Photoluminescence (PL) Spectroscopy. At room temperature using a PL spectrometer, we were able to acquire the PL emission spectra of both undoped and nickel-doped zinc oxide across the wavelength range of 200–800 nm. All the samples were excited at 340 nm. There are emission observations in two different regions: one in the ultraviolet range and the other in the visible range. PL spectra are shown in Figure 6, along with their respective nickel contents. The reason for the emission peak being observed at 395 nm [32] is because of the free exciton emission that occurs in the zinc oxide nanostructures. The transition of an electron from a narrow donor level of Zn_i to the uppermost valence band correlates to the violet absorption peak that occurs at around 412 nm [33, 39]. It is believed that singly ionized zinc or other inherent defects are responsible for the blue [4, 35] emission peak that occurs about 451 nm. There is a possibility that singly ionized oxygen defects are responsible for the peak that is found in the green spectrum about 558 nm [21]. The peaks that appear in the red [40] region around 640–680 nm are attributed to electron recombination that occurs between the donor level and the acceptor level. The donor level is associated with oxygen defects, and the acceptor level is associated with vacancies, particularly as a result of doping. The various peak shifts due to nickel doping are given in Table 3.

It was noted that in the doped samples, there are least defects in the undoped zinc oxide sample having less intense spectra, while there are a large number of vacancies in the $\text{Zn}_{0.94}\text{Ni}_{0.06}\text{O}$ sample presenting more intense emission spectrum. The various vacancies were validated by the PL emission spectra. These findings are linked to the UV-visible absorption spectra for both samples which exhibited low and high absorption, respectively, as well as the results of the SEM examination, which revealed that the rods in the $\text{Zn}_{0.94}\text{Ni}_{0.06}\text{O}$ sample did not develop properly owing to the higher nickel content.

3.6. Dielectric Properties

3.6.1. Dielectric Constant. The frequency dependence of the dielectric constant for undoped zinc oxide and nickel-doped zinc oxide that has been annealed at 600°C is shown in

Figure 7. Using a pellet presser, the produced samples were compressed into the shape of circular pellets, from which the capacitance, dielectric loss, and alternating current conductivity were measured as a function of frequency. Capacitance was measured by stacking silver paste electrodes on top of the pellets to make a circular parallel plate. To calculate the dielectric constant of both undoped and nickel-doped zinc oxide, the following equation was used:

$$\epsilon_r = \frac{Cd}{\epsilon_0 A}, \quad (7)$$

where ϵ_r is the relative permittivity, C is the capacitance, d is the pellet's width, ϵ_0 is the permittivity of free space, and A is the pellet's cross-sectional area.

The ϵ_r values of both undoped and nickel-doped zinc oxide were found to decrease with frequency up to 1×10^3 Hz. At higher frequencies, the values of ϵ_r are nearly consistent between samples. Nickel-doped samples were found to possess a higher dielectric constant than undoped zinc oxide; this value was found to be maximum in the nickel content ($x=0.06$) at low frequencies. According to the “Maxwell–Wagner” interfacial model, dielectric materials should feature a dual layer of fine transporting grains consisting of disconnected grain boundaries [38]. Nickel doping causes a large increase of oxygen vacancies, which trap charge carriers and generate massive polarization in the system, leading to a high permittivity at low frequencies. High dielectric constants are caused by both space charge polarization (SCP) and rotating directional polarization (RDP). Because of the structural inhomogeneity brought forth by the grains' high surface-to-volume ratio, interfacial polarization is enhanced. The pellets, made up of bonded nanograins, may have surface effects, oxygen voids, micropores, and other vacancy clusters. These oxygen deficiencies can be categorized into single or double states [41, 42]. When positive and negative ions bond, they create a plethora of dipole moments, each with its own random orientation that may be polarized with an external field. These dipole moments align with the direction of the applied field, causing a rotational polarization to occur (RDP). Grain boundaries become electrically active due to the capture of space charge carriers travelling in the opposite direction of the applied field by defects, mostly oxygen vacancies [43], etc., that induce SCP in the nanostructures, leading to an increase in the dielectric constant at low frequencies. The decrease in the dielectric constant at higher frequencies is caused by any species that is sensitive to polarizability falling behind the supplied field at those frequencies. Higher surface-to-volume ratios result in greater SCP and RDP because of the increased border capacity. Nickel impurities, or dopants, introduced into zinc oxide result in an increase in oxygen vacancies, which in turn boost SCP and RDP and, by extension, ϵ_r .

As expected, the $\text{Zn}_{0.94}\text{Ni}_{0.06}\text{O}$ nickel-doped zinc oxide sample has the highest dielectric constant of all the synthesized samples, with the undoped zinc oxide sample having the lowest. When the nickel content was enhanced, oxygen vacancies increased, leading to a higher dielectric

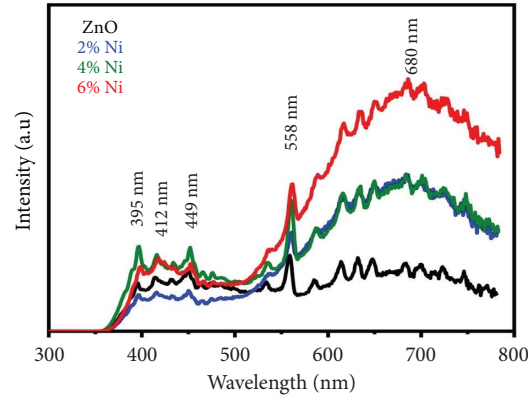


FIGURE 6: PL emission spectra of undoped and nickel-doped zinc oxide.

TABLE 3: Position of PL emission peaks of undoped and nickel doped zinc oxide.

Peak no	ZnO (nm)	Zn _{0.98} Ni _{0.02} O (nm)	Zn _{0.96} Ni _{0.04} O (nm)	Zn _{0.94} Ni _{0.06} O (nm)
1	395	396	397	398
2	412	415	416	418
3	449	450	451	453
4	558	560	561	562
5	680	684	685	688

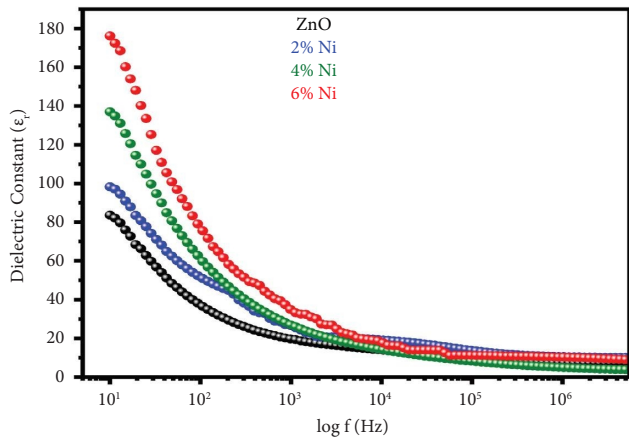


FIGURE 7: Frequency-dependent dielectric constant of undoped and nickel-doped zinc oxide.

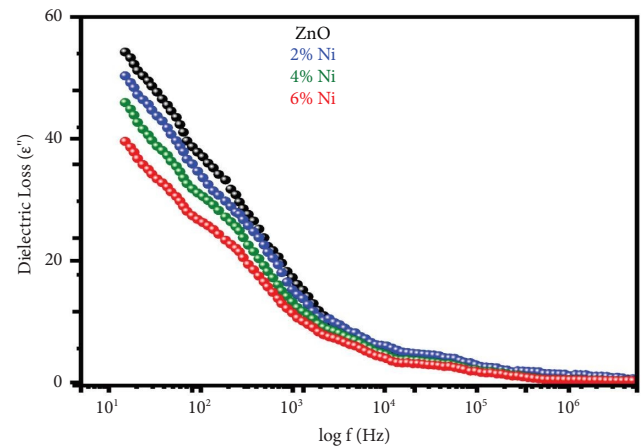


FIGURE 8: Frequency-dependent dielectric loss of undoped and nickel-doped zinc oxide.

constant. EDX and photoluminescence study indicated that the Zn_{0.94}Ni_{0.06}O nickel-doped sample contains the maximum amount of vacancies and hence displays the highest dielectric constant.

3.6.2. Dielectric Loss. Figure 8 depicts the frequency-dependent change in dielectric loss, ϵ'' , for both undoped and nickel-doped zinc oxide (nickel = 0.02, 0.04, and 0.06) nanostructures. Figure 8 gives the impression that ϵ'' decreases with increasing frequencies. Each sample exhibits scattering at low frequencies and frequency-independent behavior at high ones. Increasing frequencies may have resulted in less dielectric loss due to SCP. It is assumed that the resonance of the domain wall is responsible for inducing

the dielectric loss and for forcing the polarization to rotate. For all samples, it is found that dielectric losses are minimal at higher frequencies, which may be because the domain wall's motion is impeded. The weakening of ϵ'' at higher frequencies may also be brought on by the migration of ions within the sample. At low frequencies, it was also observed that increasing the nickel content of zinc oxide (nickel = 0.02, 0.04, and 0.06) decreased dielectric loss and increased the dielectric constant. Nickel-doped zinc oxide's constant dielectric loss at high frequencies and low dielectric loss at lower frequencies make it a useful material for high-frequency device fabrication. Ionic hopping may account for the dielectric losses at low and intermediate frequencies, while ionic migrations may account for the conduction losses.

Pure zinc oxide has the maximum dielectric loss among the synthesized samples, whereas the $\text{Zn}_{0.94}\text{Ni}_{0.06}\text{O}$ nickel-doped zinc oxide sample has the lowest dielectric constant due to its higher nickel content. As nickel concentration rose, dielectric loss reduced. The lowest dielectric loss was seen in the $\text{Zn}_{0.94}\text{Ni}_{0.06}\text{O}$ nickel-doped sample, which was validated by EDX and photoluminescence analysis to have the maximum number of vacancies, leading to greater conduction of charges.

3.6.3. Electrical Conductivity. Figure 9 depicts the electrical conductivity of undoped and nickel-doped zinc oxide nanostructures as a function of frequency for an alternating current. It is often believed, and supported by research [44], that AC electrical conductivity increases as frequency increases. The electrical conductivity of all the samples is almost nil at very low frequencies, rising steadily with increasing frequencies and then dramatically increasing at extremely high frequencies. The Maxwell–Wagner interfacial model can explain this frequency-dependent conductivity performance. The charge carriers are met with resistance at the grain boundaries. These ions are free to move about inside the grains, but their resistive nature prevents them from leaving the grains. The little increase in conductivity at low frequencies can result from the tunneling or hopping effect, and charge carriers might be transported by an endless number of pathways between grains. In order to promote conductivity, a material needs a high frequency so that the charge transporters have enough energy to overcome the barriers, freeing the charges. When nickel is introduced into the $\text{Zn}_{1-x}\text{Ni}_x\text{O}$ lattice, a significant number of charge transporters are generated, leading to an increase in conductivity. The AC conductivity of undoped and nickel-doped zinc oxide is calculated using the following formula:

$$\sigma_{a.c.} = \epsilon \epsilon'' \omega. \quad (8)$$

Since $(\omega = 2\pi f)$ f is the frequency, $(\sigma_{a.c.})$ is the electrical conductivity of alternating current, (ϵ) is the imaginary component of the dielectric constant, (ϵ_0) is the dielectric constant of free space.

Since the dielectric loss decreases with frequency while the conductivity increases, it is obvious from the preceding equation that the tangent loss alone determines the AC conductivity. This result is consistent with the literature, which demonstrates that a series of opposing effects [44] support the trend of increased $\sigma_{a.c.}$ with higher frequencies.

There are two possible explanations for this increase in AC electrical conductivity: either the electrical energy associated with a high AC frequency applied field enables charge transporters to hop between the nanostructures, or the polarization of zinc oxide nanoparticles is reduced to a greater extent at higher frequencies, making the material more dielectric. When the concentration of the dopant is increased, more oxygen vacancies are created, which bind the charge transporters. The supplied field has a lot of energy at higher frequencies, and hence the AC conductivity increases suddenly as a result of the discharge of these charges.

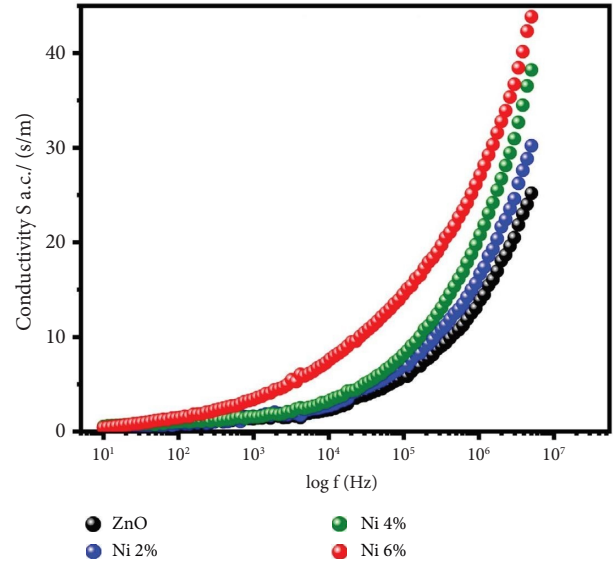


FIGURE 9: Frequency-dependent AC electrical conductivity of undoped and nickel-doped zinc oxide.

Therefore, a rise in nickel content leads to an increase in oxygen vacancies, which in turn increases the density of charge carriers and the AC conductivity of the material. When it comes to the AC conductivity of our manufactured samples, $\text{Zn}_{0.94}\text{Ni}_{0.06}\text{O}$ nickel-doped zinc oxide comes out on top, followed by $\text{Zn}_{0.96}\text{Ni}_{0.04}\text{O}$ and $\text{Zn}_{0.98}\text{Ni}_{0.02}\text{O}$ doped samples with the maximum number of oxygen vacancies, respectively, while undoped zinc oxide has the lowest.

4. Conclusion

The undoped and nickel-doped zinc oxide nanostructures were prepared by the chemical wet precipitation method. XRD analysis confirmed the only hexagonal wurtzite structure without any other impurity phase of Zn, Ni, and NiO. EDX confirmed the substitution of nickel into the host zinc oxide lattice in different concentrations. UV-Vis spectroscopy revealed that nickel was present in octahedral symmetry without disrupting the wurtzite structure, and a red shift was due to the incorporation of nickel into zinc oxide matrix. PL showed various defects density, and the red shift observed was due to the doping of nickel in the zinc oxide lattice, attributed to the sp-d exchange interactions of the localized and band electrons of the nickel. Dielectric properties showed enhancement as the dielectric constant was increased with nickel doping and the dielectric loss was decreased. AC electrical conductivity also showed increase in the nickel-doped zinc oxide. Hence, after investigating various optical and dielectric properties, nickel-doped zinc oxide may be a helpful compound for various optical and frequency-dependent applications.

Data Availability

The data used to support the findings of this study are available from the corresponding authors upon request.

Ethical Approval

This research was conducted in a legal and ethical way and is completely in compliance with the ethical standards.

Conflicts of Interest

The authors declare that they have no conflicts of interest.

Authors' Contributions

All the authors contributed equally to this work.

Acknowledgments

This study was self-funded.

References

- [1] D. Liu and T. L. Kelly, "Perovskite solar cells with a planar heterojunction structure prepared using room-temperature solution processing techniques," *Nature Photonics*, vol. 8, no. 2, pp. 133–138, 2014.
- [2] H. Zhou, Y. Zhang, C.-K. Mai et al., "Polymer Homo-tandem solar cells with best efficiency of 11.3%," *Advanced Materials*, vol. 27, no. 10, pp. 1767–1773, 2015.
- [3] V. Vohra, K. Kawashima, T. Kakara et al., "Efficient inverted polymer solar cells employing favourable molecular orientation," *Nature Photonics*, vol. 9, no. 6, pp. 403–408, 2015.
- [4] I. Ben Elkamel, N. Hamdaoui, A. Mezni, R. Ajjel, and L. Beji, "High responsivity and 1/f noise of an ultraviolet photodetector based on Ni doped ZnO nanoparticles," *RSC Advances*, vol. 8, no. 56, pp. 32333–32343, 2018.
- [5] A. Becheri, M. Dürr, P. Lo Nostro, and P. Baglioni, "Synthesis and characterization of zinc oxide nanoparticles: application to textiles as UV-absorbers," *Journal of Nanoparticle Research*, vol. 10, no. 4, pp. 679–689, 2008.
- [6] H. Guo, J. Zhou, and Z. Lin, "ZnO nanorod light-emitting diodes fabricated by electrochemical approaches," *Electrochemistry Communications*, vol. 10, no. 1, pp. 146–150, 2008.
- [7] K. N. Hui, K. S. Hui, Q. Xia et al., "Enhanced light extraction efficiency of GaN-based LED with ZnO nanorod grown on Ga-doped ZnO seed layer," *ECS Solid State Letters*, vol. 2, no. 6, pp. Q43–Q46, 2013.
- [8] X. Fang, J. Li, D. Zhao, D. Shen, B. Li, and X. Wang, "Phosphorus-doped p-type ZnO nanorods and ZnO nanorod p-n homojunction LED fabricated by hydrothermal method," *Journal of Physical Chemistry C*, vol. 113, no. 50, pp. 21208–21212, 2009.
- [9] A. Kumar Rai, L. Tuan Anh, C.-J. Park, and J. Kim, "Electrochemical study of NiO nanoparticles electrode for application in rechargeable lithium-ion batteries," *Ceramics International*, vol. 39, no. 6, pp. 6611–6618, 2013.
- [10] X.-M. Zhang, M.-Y. Lu, Y. Zhang, L.-J. Chen, Z. L. Wang, and L. Zhong, "Fabrication of a high-brightness blue-light-emitting diode using a ZnO-nanowire array grown on p-GaN thin film," *Advanced Materials*, vol. 21, no. 27, pp. 2767–2770, 2009.
- [11] A. Kolodziejczak-Radzimska and T. Jesionowski, "Zinc oxide-from synthesis to application: a review," *Materials*, vol. 7, no. 4, pp. 2833–2881, 2014.
- [12] S. Y. Lee, E. S. Shim, H. S. Kang, S. S. Pang, and J. S. Kang, "Fabrication of ZnO thin film diode using laser annealing," *Thin Solid Films*, vol. 473, no. 1, pp. 31–34, 2005.
- [13] I. Miccoli, R. Spampinato, F. Marzo, P. Prete, and N. Lovergine, "DC-magnetron sputtering of ZnO: Al films on (00.1) Al₂O₃ substrates from slip-casting sintered ceramic targets," *Applied Surface Science*, vol. 313, pp. 418–423, 2014.
- [14] O. Semong, B. S. Batlokwa, and others, "Rapid colorimetric detection of Hg (II) based on Hg (II)-Induced suppressed enzyme-like reduction of 4-nitrophenol by Au@ ZnO/Fe₃O₄ in a cosmetic skin product," *Nanomaterials and Nanotechnology*, vol. 2023, Article ID 3603680, 14 pages, 2023.
- [15] D. Huang, Z. Liu, Y. Li, and Y. Liu, "Colossal permittivity and dielectric relaxation of (Li, In) Co-doped ZnO ceramics," *Journal of Alloys and Compounds*, vol. 698, pp. 200–206, 2017.
- [16] J. Wang, R. Chen, L. Xiang, and S. Komarneni, "Synthesis, properties and applications of ZnO nanomaterials with oxygen vacancies: a review," *Ceramics International*, vol. 44, no. 7, pp. 7357–7377, 2018.
- [17] K. Jeyasubramanian, R. V. William, P. Thiruramanathan et al., "Dielectric and magnetic properties of nanoporous nickel doped zinc oxide for spintronic applications," *Journal of Magnetism and Magnetic Materials*, vol. 485, pp. 27–35, 2019.
- [18] C.-C. Tsai, S.-Y. Chu, C.-S. Hong, and S.-L. Yang, "Influence of A-site deficiency on oxygen-vacancy-related dielectric relaxation, electrical and temperature stability properties of CuO-doped NKN-based piezoelectric ceramics," *Ceramics International*, vol. 39, pp. S165–S170, 2013.
- [19] K. Chakrabarti, B. Sarkar, V. D. Ashok, S. S. Chaudhuri, and S. De, "Enhanced magnetic and dielectric behavior in Co doped BiFeO₃ nanoparticles," *Journal of Magnetism and Magnetic Materials*, vol. 381, pp. 271–277, 2015.
- [20] S. U. Haque, K. K. Saikia, G. Murugesan, and S. Kalainathan, "A study on dielectric and magnetic properties of lanthanum substituted cobalt ferrite," *Journal of Alloys and Compounds*, vol. 701, pp. 612–618, 2017.
- [21] E. Praveen and K. Jayakumar, "Investigations on structural, optical and ferromagnetic properties of Ni doped ZnO nanotwins," *Materials Science in Semiconductor Processing*, vol. 102, Article ID 104609, 2019.
- [22] Z. Manzoor, V. Saravade, A. M. Corda, I. Ferguson, and L. Lu, "Optical and structural properties of nickel doped zinc oxide grown by metal organic chemical vapor deposition (MOCVD) at different reaction chamber conditions," *ES Materials & Manufacturing*, vol. 8, pp. 31–35, 2020.
- [23] I. Benaicha, J. Mhalla, A. Raidou, A. Qachaou, and M. F. Houme, "Effect of Ni doping on optical, structural, and morphological properties of ZnO thin films synthesized by MSILAR: experimental and DFT study," *Materialia*, vol. 15, Article ID 101015, 2021.
- [24] S. Karmakar, B. Panda, B. Sahoo, K. L. Routray, S. Varma, and D. Behera, "A study on optical and dielectric properties of Ni-ZnO nanocomposite," *Materials Science in Semiconductor Processing*, vol. 88, pp. 198–206, 2018.
- [25] H. Singh, V. Kumar, H. C. Jeon, T. W. Kang, and S. Kumar, "Structural, optical and electrical properties of Ni doped ZnO nanostructures synthesized by solution combustion method," *Journal of Materials Science: Materials in Electronics*, vol. 29, no. 2, pp. 1327–1332, 2018.
- [26] M. P. Dasari, U. Godavarti, and V. Mote, "Structural, morphological, magnetic and electrical properties of Ni-doped ZnO nanoparticles synthesized by co-precipitation method," *Processing and Application of Ceramics*, vol. 12, no. 2, pp. 100–110, 2018.
- [27] M. P. Dasari, U. Godavarti, and V. Mote, "Structural, morphological, magnetic and electrical properties of Ni-doped ZnO nanoparticles synthesized by co-precipitation method,"

- Processing and Application of Ceramics*, vol. 12, no. 2, pp. 100–110, 2018.
- [28] P. Prete, N. Lovergine, and L. Tapfer, “Nanostructure size evolution during Au-catalysed growth by carbo-thermal evaporation of well-aligned ZnO nanowires on (100) Si,” *Applied Physics A*, vol. 88, no. 1, pp. 21–26, 2007.
- [29] J. K. Liang, H. L. Su, C. L. Kuo et al., “Structural, optical and electrical properties of electrode-positated Sb-doped ZnO nanorod arrays,” *Electrochimica Acta*, vol. 125, pp. 124–132, 2014.
- [30] N. Hamdaoui and L. Beji, “Electrical characterization and dielectric impedance of Au/n-CdS/p-porous GaAs/p++-GaAs thin film structures,” *Journal of Applied Physics*, vol. 121, no. 18, 2017.
- [31] I. Ben Elkamel, N. Hamdaoui, A. Mezni, and R. Ajjel, “Enhancement of dielectric properties of Ni and Co doped ZnO due to the oxygen vacancies for UV photosensors application,” *Physica E: Low-Dimensional Systems and Nanostructures*, vol. 119, Article ID 114031, 2020.
- [32] M. P. Dasari, U. Godavarti, and V. Mote, “Structural, morphological, magnetic and electrical properties of Ni-doped ZnO nanoparticles synthesized by co-precipitation method,” *Processing and Application of Ceramics*, vol. 12, no. 2, pp. 100–110, 2018.
- [33] P. Geetha Devi and A. Sakthi Velu, “Synthesis by co-precipitation method, structural and optical properties of ZnO and nickel doped ZnO nanoparticles,” *Journal of Advanced Applied Scientific Research*, vol. 1, no. 2, pp. 130–137, 2015.
- [34] K. Raja, P. S. Ramesh, and D. Geetha, “Synthesis, structural and optical properties of ZnO and Ni-doped ZnO hexagonal nanorods by Co-precipitation method,” *Spectrochimica Acta Part A: Molecular and Biomolecular Spectroscopy*, vol. 120, pp. 19–24, 2014.
- [35] S. Chattopadhyay, K. P. Misra, A. Agarwala et al., “Dislocations and particle size governed band gap and ferromagnetic ordering in Ni doped ZnO nanoparticles synthesized via co-precipitation,” *Ceramics International*, vol. 45, no. 17, pp. 23341–23354, 2019.
- [36] V. Gandhi, R. Ganesan, H. H. Abdulrahman Syedahamed, M. Thaiyan, and M. Thaiyan, “Effect of cobalt doping on structural, optical, and magnetic properties of ZnO nanoparticles synthesized by coprecipitation method,” *Journal of Physical Chemistry C*, vol. 118, no. 18, pp. 9715–9725, 2014.
- [37] G. Vijayaprasath, R. Murugan, S. Asaithambi et al., “Structural characterization and magnetic properties of Co co-doped Ni/ZnO nanoparticles,” *Applied Physics A*, vol. 122, no. 2, 2016.
- [38] L. H. Qian, X. Q. Yan, T. Fujita, A. Inoue, and M. W. Chen, “Surface enhanced Raman scattering of nanoporous gold: smaller pore sizes stronger enhancements,” *Applied Physics Letters*, vol. 90, no. 15, 2007.
- [39] D. Tamilselvi, N. Velmani, and K. Rathidevi, “Effect of ni-doping on the structural and optical properties of ZnO nanoparticles prepared by chemical precipitation method,” *Journal of Ovonic Research*, vol. 16, no. 2, pp. 123–130, 2020.
- [40] L.-N. Tong, T. Cheng, H.-B. Han et al., “Photoluminescence studies on structural defects and room temperature ferromagnetism in Ni and Ni-H doped ZnO nanoparticles,” *Journal of Applied Physics*, vol. 108, no. 2, 2010.
- [41] K. Rajwali and M.-H. Fang, “Dielectric and magnetic properties of (Zn, Co) co-doped SnO₂ nanoparticles,” *Chinese Physics B*, vol. 24, no. 12, Article ID 127803, 2015.
- [42] R. Khan, Zulfiqar, S. Fashu, and Y. Zaman, “Magnetic and dielectric properties of (Co, Zn) co-doped SnO₂ diluted magnetic semiconducting nanoparticles,” *Journal of Materials Science: Materials in Electronics*, vol. 27, no. 6, pp. 5960–5966, 2016.
- [43] F. Gu, S. F. Wang, M. K. Lü et al., “Photoluminescence properties of SnO₂ nanoparticles synthesized by sol-gel method,” *The Journal of Physical Chemistry B*, vol. 108, no. 24, pp. 8119–8123, 2004.
- [44] G. Srinet, R. Kumar, and V. Sajal, “Structural, optical, vibrational, and magnetic properties of solgel derived Ni doped ZnO Nanoparticles,” *Journal of Applied Physics*, vol. 114, no. 3, Article ID 033912, 2013.